High-Precision Surface Plasmon Resonance (SPR)-Based Five-Parameter Optical Fiber Sensor for the Simultaneous Detection of Refractive Index, Temperature, Magnetic Field, Relative Humidity, and Voltage

Weiqiang Wang, Jingwei Lv, Jianxin Wang, Miao Liu, Wei Liu, Zao Yi, Qiang Liu, Paul K. Chu, and Chao Liu

***Abstract*—A multifunctional optical fiber sensor based on surface plasmon resonance (SPR) is designed and demonstrated for the synchronous detection of refractive index (N), temperature (T), magnetic field (H), relative humidity (RH), and voltage (U). The device employs a ten-hole photonic crystal fiber (PCF) (ten-hole PCF) as the substrate. Gold (Au) films are deposited in the alternately distributed air holes, which are subsequently filled with the analyte (Anal), polydimethylsiloxane (PDMS), magnetic fluid (MF), polyvinyl alcohol (PVA), and E7 nematic liquid crystal (E7NLC), respectively. This sensor enables synchronous multiparameter detection using a single segment of the optical fiber. Numerical analysis reveals that in the ranges of 1.321.38 RIU, 20 °C-40 °C, 35-135 Oe, 30%-70%, and 180-260 V, the average refractive index sensitivity, temperature sensitivity, magnetic field sensitivity, relative humidity sensitivity, and relative voltage sensitivity are 4490.34 nm/RIU, −8.05 nm/°C, 1.52 nm/Oe, −5.83 nm/%RH, and 4.25 nm/V, respectively. Featuring a simple structure, the sensor achieves integrated five-parameter sensing for the first time. The results reveal a novel concept for multiphysical field sensing with a single segment of optical fiber.**

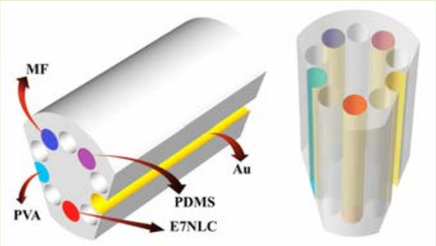

***Index Terms*— Multiparameter detection, numerical simulation, photonic crystal fiber (PCF), sensing.**

I. Introduction

SPURRED by the recent development of optical fiber technology, optical fiber sensors have become increasingly widespread. Jorgenson and Yee [1] from the University of Washington reported a multimode optical fiber chemical sensor based on surface plasmon resonance (SPR). They first proposed the SPR effect using optical fiber as a carrier and successfully applied it to gas sensing [1]. Compared with traditional electronic sensors, optical fiber sensors have the advantages of small size, high sensitivity, and fast response speed. Hence, optical fiber sensors have been used in various fields, among which those based on the principle of SPR stand out due to their unique advantages. Traditional optical fiber sensors can normally detect one variable, that is, a one-parameter type, and cannot meet the detection requirements in complex environments. The reason is that the sensing materials can be affected by multiple variables, thus giving rise to cross-sensitivity and inaccurate detection. In particular, the cross-sensitivity phenomenon is particularly significant in the detection of refractive index (N), temperature (T), magnetic field (H), relative humidity (RH), and voltage (U). Fortunately, the impact of cross-sensitivity can be abated by integrating multiple sensing materials for compensated detection. Moreover, the higher the integration level, the more significant the mitigation, and the more accurate the detection. Up to now, a single segment of optical fiber for three parameters has been proposed [2], [3], [4].

Received 8 October 2025; accepted 25 October 2025. Date of publication 5 November 2025; date of current version 15 December 2025. This work was supported in part by Heilongjiang Provincial Natural Science Foundation of China under Grant JQ2023F001, in part by the National Natural Science Foundation of China under Grant 12304480, in part by China Postdoctoral Science Foundation Funded Project under Grant 2020M670881, and in part by the City University of Hong Kong Donation Research under Grant DON-RMG 9229021 and Grant DON-RMG 9220061. The associate editor coordinating the review of this article and approving it for publication was Dr. Anand M. Shrivastav. *(Corresponding author: Chao Liu.)*

Please see the Acknowledgment section of this article for the author affiliations.

Digital Object Identifier 10.1109/JSEN.2025.3627403

del Carmen Alonso-Murias et al. [5] designed a three-parameter sensor composed of a photonic crystal fiber (PCF) for the measurement of temperature, magnetic field, and refractive index. This sensor accomplished magnetic field detection with temperature compensation using polydimethylsiloxane (PDMS) and magnetic fluid (MF). Zhang et al. [6] designed a sensor capable of synchronously measuring three parameters, i.e., temperature, magnetic field, and voltage, by placing the E7 liquid crystal doped with magnetic nanoparticles into the PCF. However, because this sensor relies on liquid crystals to detect both temperature and voltage simultaneously and cannot detect temperature independently, it is difficult to achieve temperature compensation. To solve this problem, Huo et al. [7] proposed a compact three-channel PCF sensor for the simultaneous measurement of liquid refractive index, temperature, and ambient magnetic field by filling with PDMS and MF. This sensor exhibited temperature compensation through PDMS. Although Wang et al. [8] have proposed a cascaded optical fiber sensor that can be used to detect temperature, stress, refractive index, and relative humidity, it should be noted that this sensor merely cascades four optical fiber sensors based on different principles and uses the wavelength division multiplexing technique to detect the signal changes of each part, respectively. Therefore, it should only be regarded as a simple spliced multifunctional sensor, but the detection accuracy does not improve [8].

A five-parameter sensor based on a ten-hole PCF is designed. By plating gold films on the alternately distributed air holes and filling them with the analyte (Anal), PDMS, MF, polyvinyl alcohol (PVA), and E7 nematic liquid crystal (E7NLC), respectively, a multiparameter and mutually compensated detection system is formed for the simultaneous detection of N, T, H, RH, and U. It is believed that this is the first time that the detection of five parameters: refractive index, temperature, magnetic field, relative humidity, and voltage, is demonstrated. In addition, the five-parameter ten-hole PCF sensor has a simple structure and is easy to manufacture, thus having great potential in scientific research, engineering, and industrial applications.

II. Model and Theory

Fig. 1(a) shows the initial structure of the sensor. The cladding diameter d_1 of the ten-hole PCF is 125 μm, the air hole diameter $\boldsymbol{d_2}$ is 21.25 μm, the distance from the air hole to the fiber core $\boldsymbol{l_1}$ is 43.75 μm, the gold film thickness $\boldsymbol{h}$ is 40 nm, the angle θ between adjacent air holes is 36°, and the side-polished depth $\boldsymbol{l_2}$ is fixed at $\boldsymbol{l_1}+ 0.25\boldsymbol{d_2}$. The modal characteristics of the sensor are analyzed by the finite element method, and the mesh division is shown in Fig. 1(b).

The sensor can be fabricated by the process schematically illustrated in Fig. 2. The first step is to form air holes with a preset shape in the quartz rod by ultrasonic drilling. The second step is to put the preform into a drawing tower and draw it into a ten-hole PCF with a diameter of 125 μm. The third step is to deposit a uniform gold film on the inner walls of alternately distributed air holes by chemical vapor deposition (CVD). The fourth step is to polish the side of the optical fiber with a fiber polishing machine (FPM) to open any two gold-plated air holes separated by three holes. The fifth step is to use femtosecond laser (fs Laser) micromachining to selectively fill PDMS. The same method is used to fill MF and E7NLC. The sixth step is to deposit PVA onto the opened air holes [11], [12].

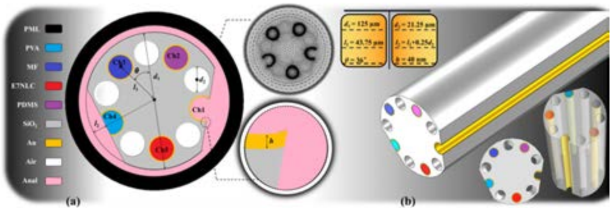

Fig. 1. (a) Cross-sectional structure and (b) grid representation of the ten-hole PCF sensor.

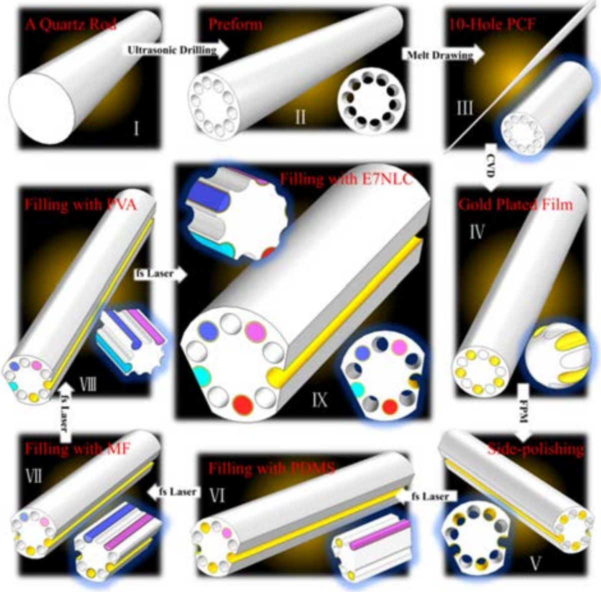

Fig. 2. Fabrication of the ten-hole PCF sensor.

The bulk material of the five-parameter ten-hole PCF sensor is fused silica. The Sellmeier equation is employed to derive n

$$n^2(\lambda, \mathrm{T}) = 1.31552 + \mathrm{A_1 T} + \frac{(\mathrm{B_1} + \mathrm{B_2 T})\,\lambda^2}{\lambda^2 - (\mathrm{B_3} + \mathrm{B_4 T})} + \frac{(\mathrm{C_1} + \mathrm{C_2 T})\,\lambda^2}{\lambda^2 - 100} \tag{1}$$

where n is the refractive index of SiO_2, λ is the wavelength of the incident light, T is the ambient temperature, $\mathrm{A_1} = 6.90754 \times 10^{-6}$, $\mathrm{B_1} = 0.788404$, $\mathrm{B_2} = 2.35835 \times 10^{-5}$, $\mathrm{B_3} = 0.0110199$, $\mathrm{B_4} = 0.584758 \times 10^{-6}$, $\mathrm{C_1} = 0.91316$, and $\mathrm{C_2} = 0.548368 \times 10^{-6}$. Gold, as a plasmonic material for the excitation of SPR, is used. Its dielectric constant can be obtained by the Drude–Lorentz model

$$\varepsilon_{\mathbf{Au}}(\boldsymbol{\omega}) = \varepsilon_1 + \mathrm{i}\varepsilon_2 = \varepsilon_\infty - \frac{\boldsymbol{\omega}_p^2}{\boldsymbol{\omega}(\boldsymbol{\omega} + \mathrm{i}\boldsymbol{\omega}_c)} \tag{2}$$

where $\boldsymbol{\varepsilon_1}$ and ε_2 are the real and imaginary parts of the metal dielectric constant, respectively, $\varepsilon_\infty = 9.48$ is the dielectric constant of gold at high frequencies, ω is the angular frequency of the incident light, $\omega_p = 1.36 \times 1016$ rad/s represents the angular frequency of the plasma, and $\omega_c = 1.45 \times 1014$ rad/s represents the damping frequency.

Voltage sensing is achieved by placing E7NLC in the air holes. The n value of E7NLC is affected not only by the voltage but also by the combined action of T and H [11], [12]. The influence can be calculated using Δn [13], [14]

$$\Delta n = \frac{\Delta \boldsymbol{\varepsilon}_{\mathbf{0}} \Delta x_{\mathbf{0}} \mathrm{H}^2}{9\mathbf{a}_{\mathbf{0}} \left(\mathrm{T} - \mathrm{T}{*}\right) \sqrt{\bar{\varepsilon}}} \tag{3}$$

where $\Delta\varepsilon_{\mathbf{0}}$ is the anisotropy of the saturated dielectric and $\bar{\varepsilon}$ is the isotropic part of the dielectric constant.

The refractive index of E7NLC is mainly affected by U

$$\mathbf{E}_{\mathbf{C}} \approx \frac{\pi}{\mathbf{d}}\sqrt{\frac{\mathbf{K}_{\mathbf{11}}}{\Delta\varepsilon}}, \boldsymbol{\theta} = \begin{cases} 0, & \mathrm{U} \le \mathrm{U}c \\ \dfrac{\pi}{2} - 2\tan^{-1}\left[\exp\left(-\dfrac{\mathrm{U}-\mathrm{U}_c}{30\mathrm{U}_c}\right)\right], & \mathrm{U} \ge \mathrm{U}_c \end{cases} \tag{4}$$

where $\boldsymbol{E}_{\mathbf{C}}$ is the threshold electric field. Under the action of this electric field, the E7NLC molecules deflect by an angle of θ along the X-axis. $\Delta\varepsilon$ represents the difference in dielectric constants. Under an electric field with a frequency of 1 kHz, $\Delta\varepsilon = 12.7$ and $\boldsymbol{k}_{\mathbf{11}} = 11.1$pn ($\boldsymbol{k}_{\mathbf{11}}$ is the splay elastic constant) [14], [15], [16].

The refractive index of E7NLC can be summarized as the ordinary refractive index no, and the extraordinary refractive index, n_o and n_e, can be calculated using the following Cauchy models [17], [18]:

$$\begin{cases} n_o = \mathbf{A}_o + \left(\dfrac{\mathbf{B}_o}{\boldsymbol{\lambda}^2}\right) + \left(\dfrac{\mathbf{C}_o}{\boldsymbol{\lambda}^4}\right) \\ n_e = \mathbf{A}_e + \left(\dfrac{\mathbf{B}_e}{\boldsymbol{\lambda}^2}\right) + \left(\dfrac{\mathbf{C}_e}{\boldsymbol{\lambda}^4}\right) \end{cases}$$
$$\begin{cases} n_x = n_o \\ n_y = \left(\dfrac{\sin^2(\boldsymbol{\theta})}{n_e^2} + \dfrac{\cos^2(\boldsymbol{\theta})}{n_o^2}\right)^{-\frac{1}{2}}. \end{cases} \tag{5}$$

The influence of T on the refractive index of E7NLC is mainly reflected in the difference of Cauchy coefficients, where $\mathbf{A}_o$, $\mathbf{B}_o$, $\mathbf{C}_o$, $\mathbf{A}_e$, $\mathbf{B}_e$, and $\mathbf{C}_e$ are the fitting coefficients of the Cauchy model [15]. Under the combined effect, the calculation formula for the n-value of E7NLC is as follows [17]:

$$n_{\mathrm{U}} = \sqrt{\frac{n_x^2 + n_y^2}{3}}, \quad n_{\mathbf{E7NLC}} = n_{\mathrm{U}} + \Delta n. \tag{6}$$

MF, a sensing material, is widely used in magnetic field detection. By applying the Langevin model, the refractive index of MF can be calculated [19]

$$n_{\mathbf{MF}} = \left(n_s - n_p\right)\left[\coth\left(\alpha\frac{\mathrm{H}-\mathrm{H}_{c,n}}{\mathrm{T}}\right) - \frac{\mathrm{T}}{\alpha\left(\mathrm{H}-\mathrm{H}_{c,n}\right)}\right] + n_p \tag{7}$$

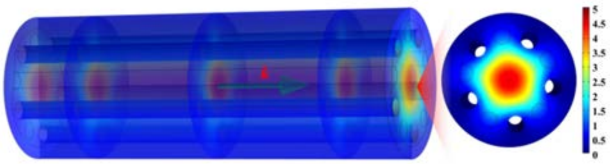

Fig. 3. 3-D electric field distribution map of y-pol FM.

where $n_p = 1.4352$ is the initial refractive index of MF, $n_s = 1.4385$ represents the saturated refractive index of MF, $\mathbf{H}_{c,n} = 30$ Oe is the magnetic field threshold, and $\alpha = 5$ is the fitting coefficient.

PVA is a humidity-sensitive material. Since PVA contains hydrophilic hydroxyl groups, it expands after absorbing water, and the refractive index changes with RH according to the following equation [20], [21]:

$$n_{\mathbf{PVA}} = -3 \times 10^{-6}\mathrm{RH}^2 - 10^{-4}\mathrm{RH} + 1.4738. \tag{8}$$

The refractive index of PDMS is only affected by temperature and exhibits a linear relationship with temperature, as shown in the following [22]:

$$n_{\mathbf{PDMS}} = -4.5 \times 10^{-4}\mathrm{T} + 1.4176. \tag{9}$$

To summarize, the multiparameter optical fiber sensor can detect N, T, H, RH, and U simultaneously. By calculating the sensitivity of each channel ($\boldsymbol{i} = 1$–5) and using the sensitivity matrix, the accurate optical fiber sensing calibration can be achieved. The specific formulas are as follows:

$$S_{\mathbf{i}}(\mathbf{X}) = \frac{\Delta\boldsymbol{\lambda}_{\mathbf{peak}\boldsymbol{i}}}{\Delta\mathbf{X}} \tag{10}$$

and

$$\begin{bmatrix} \Delta\mathrm{RW}_{\mathbf{1}} \\ \Delta\mathrm{RW}_{\mathbf{2}} \\ \Delta\mathrm{RW}_{\mathbf{3}} \\ \Delta\mathrm{RW}_{\mathbf{4}} \\ \Delta\mathrm{RW}_{\mathbf{5}} \end{bmatrix} = \begin{bmatrix} \mathbf{S}_{\mathbf{1}}(\mathrm{N}) & \mathbf{S}_{\mathbf{1}}(\mathrm{T}) & \mathbf{S}_{\mathbf{1}}(\mathrm{H}) & \mathbf{S}_{\mathbf{1}}(\mathrm{RH}) & \mathbf{S}_{\mathbf{1}}(\mathrm{U}) \\ \mathbf{S}_{\mathbf{2}}(\mathrm{N}) & \mathbf{S}_{\mathbf{2}}(\mathrm{T}) & \mathbf{S}_{\mathbf{2}}(\mathrm{H}) & \mathbf{S}_{\mathbf{2}}(\mathrm{RH}) & \mathbf{S}_{\mathbf{2}}(\mathrm{U}) \\ \mathbf{S}_{\mathbf{3}}(\mathrm{N}) & \mathbf{S}_{\mathbf{3}}(\mathrm{T}) & \mathbf{S}_{\mathbf{3}}(\mathrm{H}) & \mathbf{S}_{\mathbf{3}}(\mathrm{RH}) & \mathbf{S}_{\mathbf{3}}(\mathrm{U}) \\ \mathbf{S}_{\mathbf{4}}(\mathrm{N}) & \mathbf{S}_{\mathbf{4}}(\mathrm{T}) & \mathbf{S}_{\mathbf{4}}(\mathrm{H}) & \mathbf{S}_{\mathbf{4}}(\mathrm{RH}) & \mathbf{S}_{\mathbf{4}}(\mathrm{U}) \\ \mathbf{S}_{\mathbf{5}}(\mathrm{N}) & \mathbf{S}_{\mathbf{5}}(\mathrm{T}) & \mathbf{S}_{\mathbf{5}}(\mathrm{H}) & \mathbf{S}_{\mathbf{5}}(\mathrm{RH}) & \mathbf{S}_{\mathbf{4}}(\mathrm{U}) \end{bmatrix} \times \begin{bmatrix} \Delta\mathrm{N} \\ \Delta\mathrm{T} \\ \Delta\mathrm{H} \\ \Delta\mathrm{RH} \\ \Delta\mathrm{U} \end{bmatrix} \tag{11}$$

where $\boldsymbol{S}_{\mathbf{i}}(\boldsymbol{X})$ represents the sensitivity of the ith ($i = 1$–5) loss peak with respect to $\boldsymbol{X}$ ($\boldsymbol{X}$ representing N, T, H, RH, or U, respectively), $\Delta\mathrm{RW}\boldsymbol{i}$ ($\boldsymbol{i} = 1$–5) denotes the offset of the ith loss peak, and ΔN, ΔT, ΔH, ΔRH, and ΔU correspond to the variations of N, T, H, RH, and U, respectively. By inversely solving the matrix (11), the variations of N, T, H, RH, and U

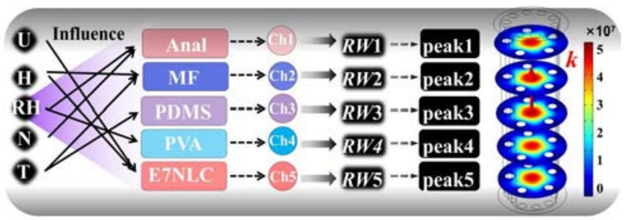

Fig. 4. Cross-interaction relationships between field quantities and sensitive materials.

can be obtained

$$\begin{bmatrix} \Delta N \\ \Delta T \\ \Delta H \\ \Delta RH \\ \Delta U \end{bmatrix} = \begin{bmatrix} \mathbf{S_1}\,(N) & \mathbf{S_1}\,(T) & \mathbf{S_1}\,(H) & \mathbf{S_1}\,(RH) & \mathbf{S_1}\,(U) \\ \mathbf{S_2}\,(N) & \mathbf{S_2}\,(T) & \mathbf{S_2}\,(H) & \mathbf{S_2}\,(RH) & \mathbf{S_2}\,(U) \\ \mathbf{S_3}\,(N) & \mathbf{S_3}\,(T) & \mathbf{S_3}\,(H) & \mathbf{S_3}\,(RH) & \mathbf{S_3}\,(U) \\ \mathbf{S_4}\,(N) & \mathbf{S_4}\,(T) & \mathbf{S_4}\,(H) & \mathbf{S_4}\,(RH) & \mathbf{S_4}\,(U) \\ \mathbf{S_5}\,(N) & \mathbf{S_5}\,(T) & \mathbf{S_5}\,(H) & \mathbf{S_5}\,(RH) & \mathbf{S_4}\,(U) \end{bmatrix}^{-1} \times \begin{bmatrix} \Delta RW_1 \\ \Delta RW_2 \\ \Delta RW_3 \\ \Delta RW_4 \\ \Delta RW_5 \end{bmatrix}. \tag{12}$$

The sharpness of the loss peak, an important indicator to evaluate the degree of optimization of the sensor, is calculated as follows [19]:

$$\mathbf{SHP} = \frac{\mathbf{Loss}}{\mathbf{FWHM}}\left(\mathrm{dB}/\mu\mathrm{m}^2\right) \tag{13}$$

where SHP is the sharpness of the loss peak and FWHM represents the full-width at half-maximum of the loss peak. The larger the value of SHP, the higher the resolution of the sensor.

The wavelength corresponding to the maximum value of the loss peak is called the resonant wavelength (RW). The optical wave loss can be calculated using the following formula [17]:

$$\boldsymbol{\alpha}_{\mathbf{Loss}} = 8.686 \times \frac{2\pi}{\boldsymbol{\lambda}} \mathrm{Im}\,(n_{\mathbf{eff}}) \times 10^7\ (\mathrm{dB/cm}) \tag{14}$$

where λ is the wavelength of the incident light and Im($n_{\mathbf{eff}}$) is the imaginary part of the effective refractive index.

The refractive indices of E7NLC and PVA are higher than that of fused silica in optical fibers. However, the air holes significantly reduce the refractive index of the cladding region. Numerical analysis shows that the sensor can confine light waves within the fiber core to achieve total reflection propagation. Fig. 3 presents the 3-D electric field distribution of the y-pol fundamental mode (FM) in the sensor.

Fig. 4 illustrates the interaction relationships between N, T, H, RH, U, and the sensitive substance. n of E7NLC is affected by T, H, and U, while that of MF is affected by T and H, and that of PVA is affected by T and RH. By selecting the PDMS material that is only sensitive to temperature, we achieve progressive compensation detection of field quantities.

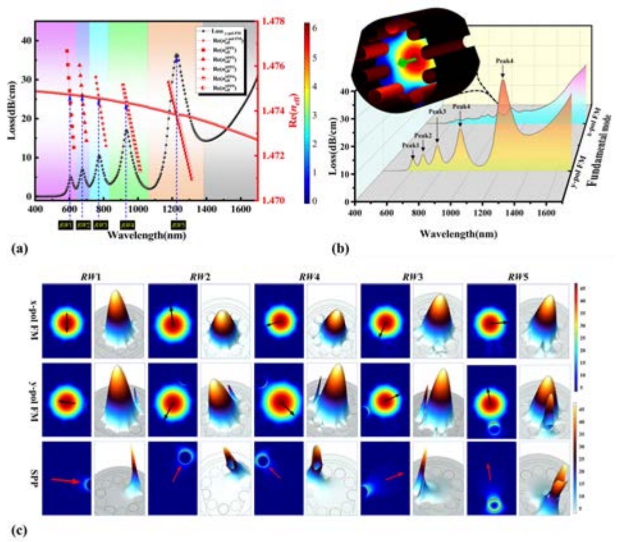

Fig. 5. (a) Loss spectra of the y-pol FM and Re(neff) for y-pol FM and SPP. (b) Loss spectra of the x-pol FM and y-pol FM. (c) Electric field distributions and 3-D mode field distribution models for x-pol FM, y-pol FM, and SPP mode.

After filling of sensitive substances with different properties, the sensor does not have rotational symmetry, and it is necessary to compare and analyze the modal characteristics of the x-polarized fundamental mode (x-pol FM) and the y-polarized fundamental mode (y-pol FM).

Fig. 5 shows the spectral characteristics of the sensor for N = 1.38, T = 25 °C, H = 60 Oe, RH = 50%, and U = 200 V. There are five significant peaks at the wavelengths of 610, 675, 775, 933, and 1225 μm. In addition, the $n_{\mathbf{eff}}$ curves of the y-pol FM and the surface plasmon polariton (SPP) mode intersect at these points, indicating that the phase matching condition is satisfied at these five specific wavelengths for the excitation of SPR. It can be seen from Fig. 4(b) that the x-pol FM shows relatively gentle changes, and therefore, it is not suitable for analyzing its spectral characteristics. Fig. 4(c) shows the mode field diagrams of the x-pol FM, y-pol FM, and SPP mode at RW$\boldsymbol{i}$ (= 1–5).

Fig. 6(a) shows that peak1 shifts significantly to red as N increases, so peak1 can uniquely detect the refractive index. Fig. 6(b) shows that only when T increases, peak2 shifts significantly to blue, and peak2 can uniquely detect temperature. Similarly, peak3 can be used to detect H, peak4 for RH, and peak5 for U.

III. STRUCTURAL OPTIMIZATION

To improve the sensing properties, the important structural parameters of the five-parameter ten-hole PCF sensor are optimized step by step from the inside of the fiber core outward. $\boldsymbol{l_2}$ is fixed at 125 μm and $\boldsymbol{l_1} + 0.25\boldsymbol{d_2}$, respectively. Since the sensor needs to detect five parameters simultaneously, numerical analysis shows that improving the sensitivity of some parameters is accompanied by a decrease in the sensitivity of other parameters. As shown in Fig. 7, with the increase of the $\boldsymbol{d_2}$ value, the sensitivities to temperature, relative humidity, and voltage increase, while the sensitivities to refractive index and magnetic field decrease. Therefore,

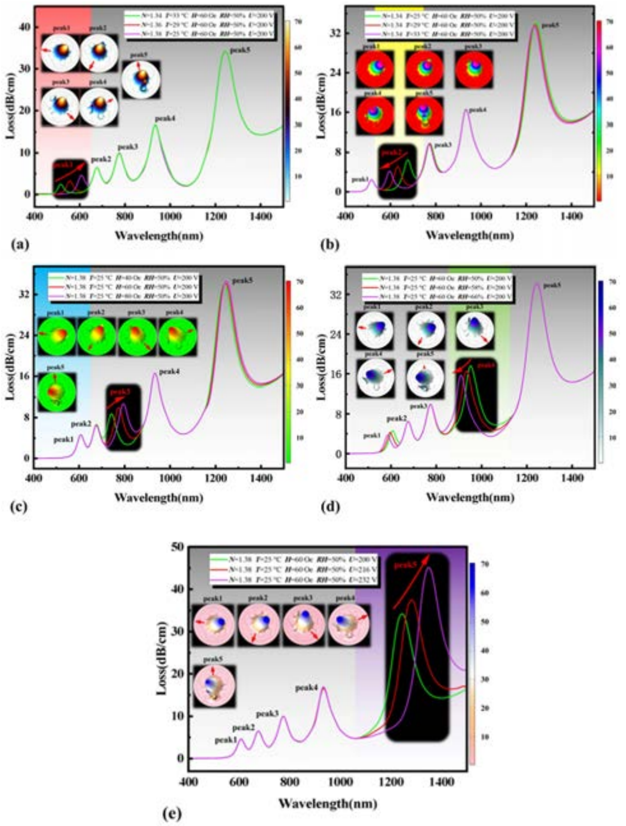

Fig. 6. (a)–(e) Relationship between the loss spectrum of y-pol FM and N, T, H, RH, and U.

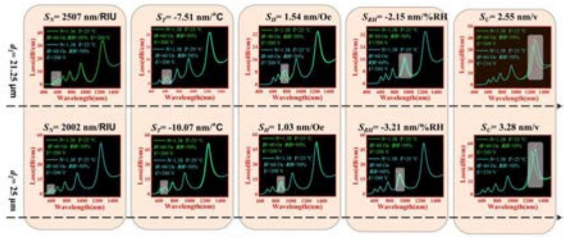

Fig. 7. Changes in sensitivity of the four loss peaks as d_2 varies from 20.5 to 25 μm.

using sensitivity as the optimization criterion lacks universality and persuasiveness. Instead, we optimize the total sharpness (S_{SUM}), total spacing (T_{SP}), and total loss (S_{Loss}) of the five resonance peaks. Specifically, $S_{\text{SUM}} = \sum_{i=1}^{5} S_{\text{HPi}}$, where S_{HPi} is the sharpness of the ith resonance peak; $\text{T}_{\text{SP}} = \text{RW5} - \text{RW1}$. The larger the S_{SUM} value, the higher the detection accuracy; the larger the T_{SP} value, the wider the detection range of the sensor; the larger the S_{Loss} value, the higher the transmission efficiency.

A. Optimization of Air Hole Radius

d_2 is optimized within the range of 10–25 μm. If d_2 is less than 10 μm, the loss spectrum no longer exhibits five obvious loss peaks, and if d_2 exceeds 25 μm, the spacing between air holes is too small and prone to mechanical breaking during fiber drawing. Fig. 8(a) compares the 3-D models of the sensor for different d_2 values and Fig. 8(b) compares the loss spectra of y-pol FM for different d_2 values. As d_2 increases, red-shifting of the spectral lines occurs because when d_2 increases, n_{eff} of the fiber core decreases, in turn decreasing n_{eff} of y-pol FM. According to the optical formulas: $n = c/v$ and $\lambda = v/f$ (where c is the speed of light in vacuum, **v** is the speed of light in the medium, and **f** is the intrinsic frequency of light, which is constant), a smaller n_{eff} increases the wavelength λ and red-shifts. Fig. 8(c) shows the electric field distributions for the five resonance wavelengths to visually compare the coupling. Fig. 8(d) shows the variation trends of S_{Loss}, T_{SP}, and S_{SUM} of the five loss peaks with d_2. When d_2 is 25 μm, the S_{SUM} and T_{SP} of the sensor reach their maximum, but the loss increases accordingly. After a comprehensive evaluation, d_2 is selected to be 21.25 μm.

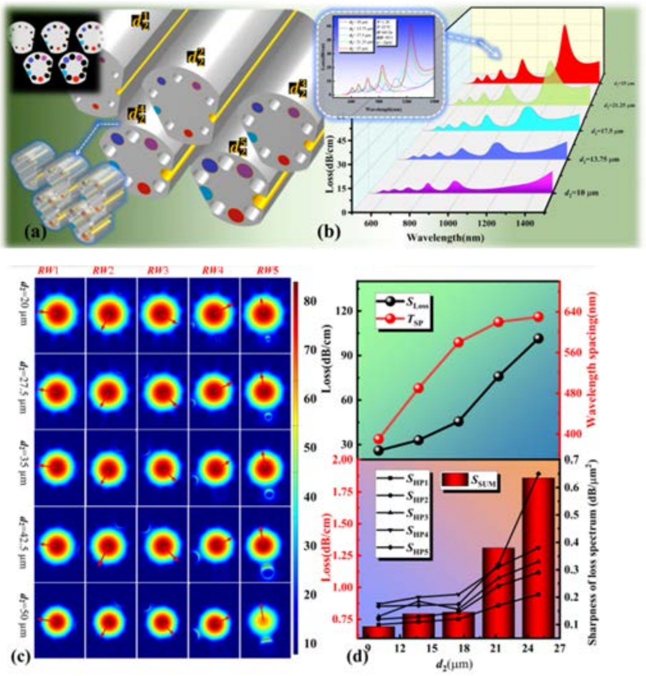

Fig. 8. For d_2 between 10 and 25 μm. (a) 3-D model of the sensor. (b) Loss spectra of y-pol FM. (c) Electric field distributions and height diagrams for the five resonance wavelengths. (d) Variations of $\mathbf{S}_{\text{Loss}}$, $\mathbf{S}_{\text{SUM}}$, and T_{SP} of the five loss peaks.

B. Optimization of Air-Hole Position

The optimization process of air hole positions is as shown in Fig. 9(a)–(d). With d_2 set to 21.25 μm, l_1 is optimized within the range of 37.5–50 μm. If l_1 is less than 37.5 μm, the spacing between air holes becomes too small, and if l_1 is greater than 50 μm, the sensor no longer exhibits obvious loss peaks. It can be observed that the loss spectra hardly shift. The refractive index distribution of the fiber cross section has a fan shape along with the filled holes. When the size of the air holes is fixed and their positions change radially, the refractive index difference between the fiber core and the filled regions remains almost unchanged, resulting in no significant shift in the loss spectra.

The peak of the loss spectrum decreases as l_1 increases. This is because a smaller l_1 shortens the distance between the gold film and the fiber core, making it easier for the y-pol FM and SPP modes to couple, thereby giving rise to a greater loss. When l_1 is 37.5 μm, the sharpness is optimal and the loss is low; therefore, l_1 is set to 37.5 μm.

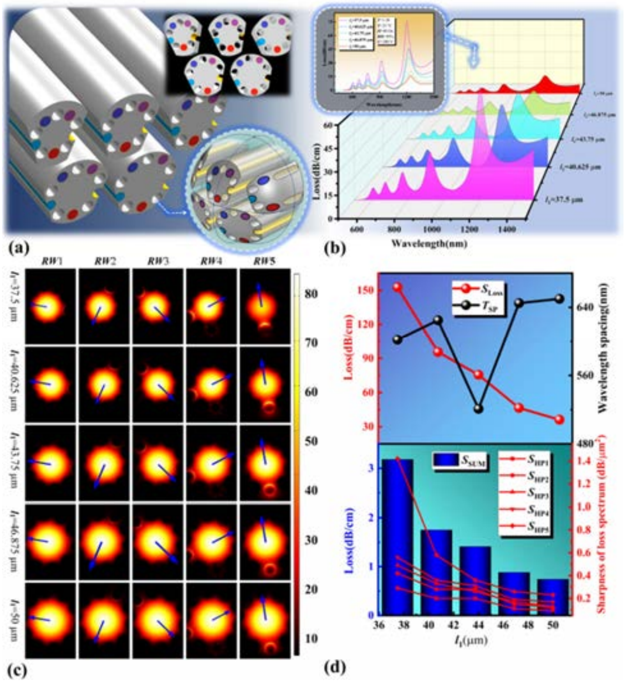

Fig. 9. For l_1 between 37.5 and 50 μm. (a) 3-D model of the sensor. (b) Loss spectra of y-pol FM. (c) Electric field distributions and height diagrams for the five resonance wavelengths. (d) Variations of **SL**$_{\text{oss}}$, **S**$_{\text{SUM}}$, and T$_{\text{SP}}$ of the four loss peaks.

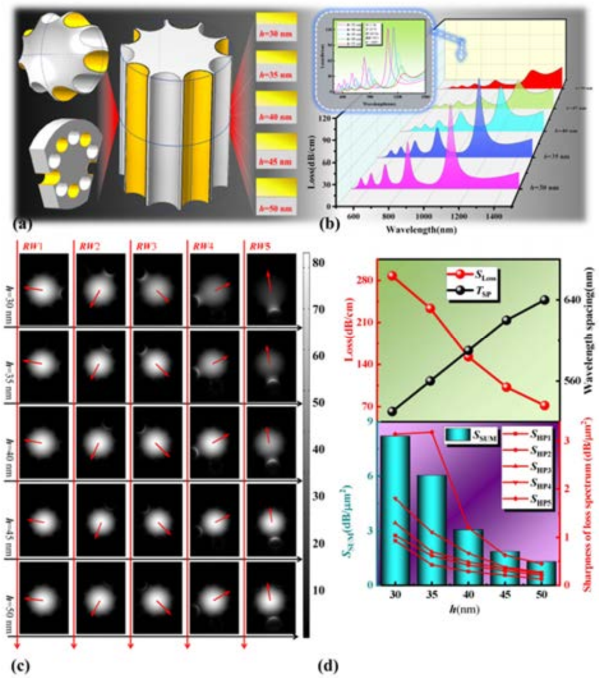

Fig. 10. For h between 30 and 50 nm. (a) 3-D model of the sensor. (b) Loss spectra of y-pol FM. (c) Electric field distributions and height diagrams for the five resonance wavelengths. (d) Variation of SLoss, SSUM, and TSP of the four loss peaks.

C. Optimization of Gold Film Thickness

With d_2 being 21.25 μm and l_1 being 37.5 μm, h is optimized within the range of 30–50 nm. When h is less than 30 nm, the coating process becomes more difficult and the loss is excessive. When h is greater than 50 nm, it is impossible to excite loss peaks. Fig. 10(a) shows the 3-D model, and Fig. 10(b) compares the loss spectra of the y-pol FM. As h increases, the loss spectrum shows red shifts. When the wavelength is between 600 and 2000 nm, the refractive index of gold is about 0.6 RIU and significantly lower than that of the optical fiber. Therefore, increasing h decreases the average refractive index near the gold film and n_{eff} of the SPP mode. As mentioned earlier, $v = c/n$ and $\lambda = v/f$, and so, λ increases, that is, red shift. It can be observed that the peak spacing changes slightly, and the loss decreases as h increases. This phenomenon can be explained by the electric field diagrams in Fig. 10(c). A smaller h produces more obvious coupling between the y-pol FM and the SPP mode, meaning that more energy is coupled to the filled area and a higher loss. When h is 30 nm, the sharpness reaches its maximum, and the sensor shows the best detection accuracy as well. Considering various factors comprehensively, h is selected to be 30 nm.

Fig. 11 shows the 3-D model of the optimized sensor with $d_1 = 125$ μm, $d_2 = 21.25$ μm, $l_1 = 37.5$ μm, $l_2 = l_1 + 0.25d_2$, $\theta = 36°$, and $h = 30$ nm.

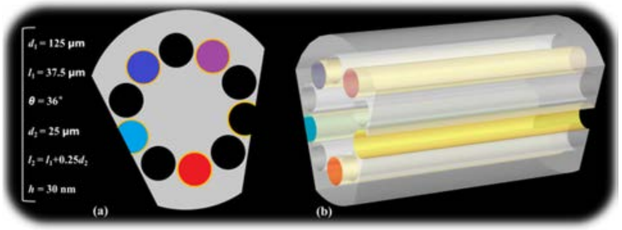

Fig. 11. (a) Optimized sensor cross-section. (b) Optimized sensor 3-D model.

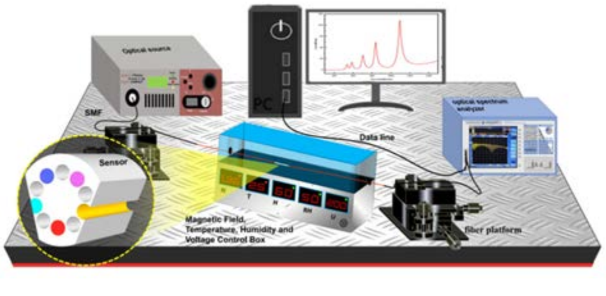

Fig. 12. Schematic of the apparatus for the measurement of refractive index, temperature, magnetic field, relative humidity, and voltage.

IV. SENSING PLATFORM AND CHARACTERISTICS

The sensor synchronously detects the refractive index, temperature, magnetic field, relative humidity, and voltage using the apparatus depicted in Fig. 12. The SMF is spliced at both ends using a fiber fusion splicer, and the SMF transmits the optical signals. A control box is used to simulate the environment with a specific refractive index, temperature, magnetic field, relative humidity, and voltage. The broadband light source provides the optical signals required for the desired band, and an optical spectrum analyzer (OSA) converts the optical signals into electrical signals and modulates them. The modulated electrical data are then analyzed by a computer.

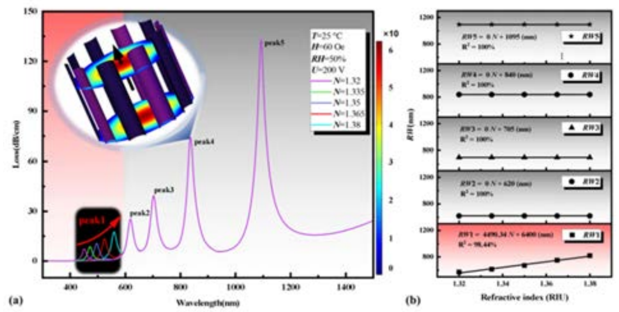

Fig. 13. (a) Loss spectra of y-pol FM for different N (1.32–1.38 RIU) and (b) RW linear fitting.

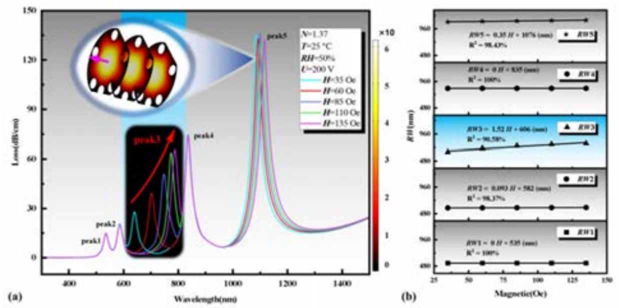

Fig. 15. (a) Loss spectra of y-pol FM for different H (35–135 Oe) and (b) RW linear fitting.

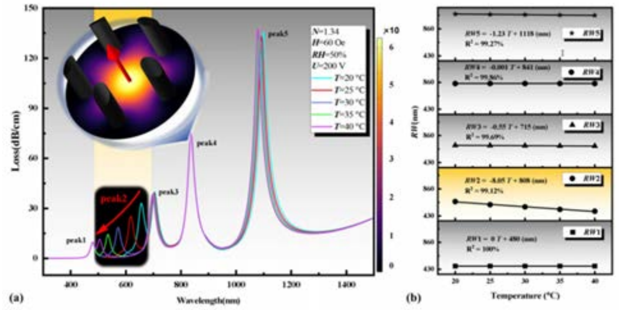

Fig. 14. (a) Loss spectra of y-pol FM for different T (20 °C–40 °C) and (b) RW linear fitting.

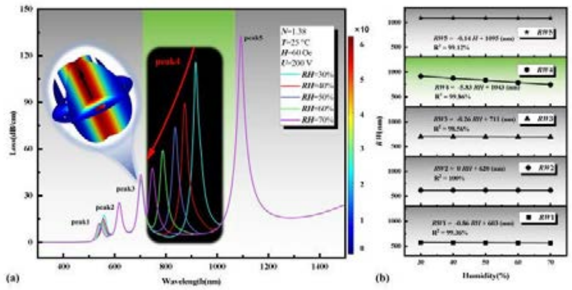

Fig. 16. (a) Loss spectra of y-pol FM for different RH (30%–70%) and (b) RW linear fitting.

The refractive index sensing characteristics of the optimized sensor are shown in Fig. 13. The loss spectra of the y-pol FM are derived as N varies uniformly in the range of 1.32–13.8 RIU. As shown in Fig. 13(a), peak1 shows an obvious shift. As shown in Fig. 13(b), the average sensitivity of each peak is calculated by linearly fitting the RW of each peak. The fitting curves of peak ***i*** (***i*** = 1–5) are: RW**1** = 4490.34 N + 6400 (nm) with a coefficient of determination (R^2) of 98.44%, RW**2** = 620 (nm) with R^2 = 100%, RW**3** = 705 (nm) with R^2 = 100%, RW**4** = 840 (nm) with R^2 = 100%, and RW**5** = 1095 (nm) with R^2 = 100%. The average refractive index sensitivities of peak ***i*** (***i*** = 1–5) are 4490.34, 0, 0, 0, and 0 nm/RIU, respectively.

Fig. 14 shows the temperature sensing characteristics of the optimized sensor. The loss spectra of the y-pol FM are derived with T varied uniformly in the range of 20 °C–40 °C. As shown in Fig. 14(a), peak2 exhibits an obvious shift. As shown in Fig. 14(b), the fitting curves of peak ***i*** (***i*** = 1–5) are: RW**1** = 480 (nm) with R^2 = 100%, RW**2** = −8.05 T + 808 (nm) with R^2 = 99.12%, RW**3** = −0.55 T+ 715 (nm) with R^2 = 99.69%, RW**4** = −0.001 T + 841 (nm) with R^2 = 99.86%, and RW**5** = −1.23 T + 1118 (nm) with R^2 = 99.27%. The average temperature sensitivities of peak ***i*** (***i*** = 1–5) are 0, −8.05, −0.55, −0.001, and −1.23 nm/°C, respectively.

The magnetic field sensing characteristics of the optimized sensor are shown in Fig. 15. The loss spectra of the y-pol FM are generated with H varied uniformly in the range of 35–135 Oe. As shown in Fig. 15(a), peak3 shows an obvious shift. As shown in Fig. 15(b), the fitting curves of peak ***i*** (***i*** = 1–5) are: RW**1** = 535 (nm) with R^2 = 100%, RW**2** = 0.093 H + 582 (nm) with R^2 = 98.37%, RW**3** = 1.52 H + 606 (nm) with R^2 = 90.58%, RW**4** = 835 (nm) with R^2 = 100%, and RW**5** = 0.35 H + 1076 (nm) with R^2 = 98.43%. The average magnetic field sensitivities of peak ***i***(***i*** = 1–5) are 0, 0.093, 1.52, 0, and 0.35 nm/Oe, respectively.

The relative humidity sensing characteristics of the optimized sensor are shown in Fig. 16. The loss spectra of the y-pol FM are derived with RH varied uniformly in the range of 30%–70%. As shown in Fig. 16(a), peak4 exhibits an obvious shift. As shown in Fig. 16(b), the fitting curves of peak ***i*** (***i*** = 1–5) are: RW**1** = −0.86RH + 603 (nm) with R^2 = 99.36%, RW**2** = 620 (nm) with R^2 = 100%, RW**3** = −0.26RH + 711 (nm) with R^2 = 98.56%, RW**4** = −5.83 RH + 1043 (nm) with R^2 = 99.86%, and RW**5** = −0.14RH + 1095 (nm) with R^2 = 99.12%. The average humidity sensitivities of peak ***i*** (***i*** = 1–5) are −0.48, 0, −0.26, −5.83, and −0.14 nm/%RH, respectively.

The voltage sensing characteristics of the optimized sensor are shown in Fig. 17. The loss spectra of y-pol FM are generated for U varied uniformly in the range of 180–260 V. As shown in Fig. 17(a), peak5 shifts significantly. As shown in Fig. 17(b), the fitting curves of peak ***i*** (***i*** = 1–5) are: RW**1** = 560 (nm), R^2 = 100%; RW**2** = 620 (nm), R^2 = 100%; RW**3** = 0.08 U + 705 (nm), R^2 = 99.45%; RW**4** = 835 (nm), R^2 = 100%; and RW**5** = 4.25 U + 302 (nm), R^2 = 99.63%. The average voltage sensitivities of peak ***i*** (***i*** = 1–5) are 0, 0, 0.08, 0, and 4.25 nm/V, respectively.

By substituting the average sensitivities of peak1, peak2, peak3, peak4, and peak5 into (12), the following five-parameter sensitivity sensing matrix can be obtained. By calculating the offset of the five resonance wavelengths,

$$\begin{bmatrix} \Delta N \\ \Delta T \\ \Delta H \\ \Delta RH \\ \Delta U \end{bmatrix} = \begin{bmatrix} 4490.34\ \text{nm/RIU} & 0\text{nm/}^\circ\text{C} & 0\ \text{nm/Oe} & -0.86\ \text{nm/\%RH} & 0\ \text{nm/V} \\ 0\text{nm/RIU} & -8.05\ \text{nm/}^\circ\text{C} & 0.093\ \text{nm/Oe} & 0\ \text{nm/\%RH} & 0\ \text{nm/V} \\ 0\text{nm/RIU} & -0.55\ \text{nm/}^\circ\text{C} & 1.52\ \text{nm/Oe} & -0.26\ \text{nm/\%RH} & 0.08\ \text{nm/V} \\ 0\text{nm/RIU} & -0.001\ \text{nm/}^\circ\text{C} & 0\ \text{nm/Oe} & -5.83\ \text{nm/\%RH} & 0\ \text{nm/V} \\ 0\ \text{/RIU} & -1.23\ \text{nm/}^\circ\text{C} & 0.35\ \text{nm/Oe} & -0.14\ \text{nm/\%RH} & 4.25\ \text{nm/V} \end{bmatrix}^{-1} \begin{bmatrix} \Delta RW_1 \\ \Delta RW_2 \\ \Delta RW_3 \\ \Delta RW_4 \\ \Delta RW_5 \end{bmatrix}$$

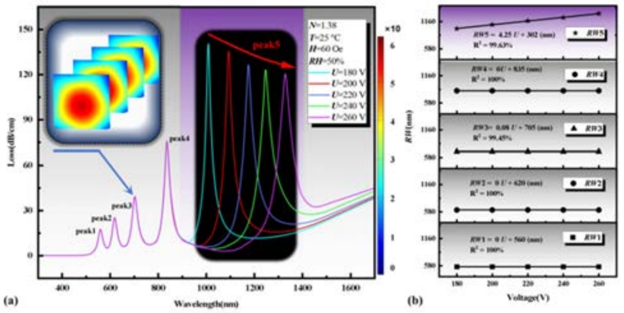

Fig. 17. (a) Loss spectra of y-pol FM for different U (180–260 V) and (b) RW linear fitting.

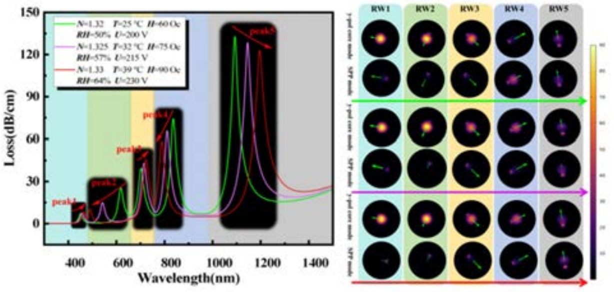

Fig. 18. Loss spectra when N, T, H, RH, and U change simultaneously.

the changes in refractive index, temperature, magnetic field, relative humidity, and voltage can be demodulated, respectively ΔN–ΔU, as shown at the top of the page.

Fig. 18 shows the simulated characteristics of the sensor as the five entities vary simultaneously.

V. CONCLUSION

A five-parameter multiphysical field optical fiber sensor composed of ten-hole PCF is designed and demonstrated to simultaneously detect the refractive index, temperature, magnetic field, relative humidity, and voltage. The sensor uses gold as the plasmonic medium to excite SPR, while PDMS, MF, PVA, and E7NLC serve as the sensing materials for N, T, H, RH, and U, respectively. The optimized structural parameters: $\boldsymbol{d_1} = 125\ \mu\text{m}$, $\boldsymbol{d_2} = 25\ \mu\text{m}$, $\boldsymbol{l_1} = 37.5\ \mu\text{m}$, $\boldsymbol{l_2} = 8.5625\ \mu\text{m}$, $\theta = 36^\circ$, and $\boldsymbol{h} = 30$ nm. Numerical analysis reveals that in the ranges of $1.32-1.38$ RIU, 20 °C–40 °C, 35–135 Oe, 30%RH–70%RH, and 180–260 V, the sensor shows an average refractive index sensitivity of 4490.34 nm/RIU, an average temperature sensitivity of −8.05 nm/°C, an average magnetic field sensitivity of 1.52 nm/Oe, an average relative humidity sensitivity of −5.83 nm/%RH, and an average voltage sensitivity of 4.25 nm/V. Boasting a simple structure, this sensor accomplishes simultaneous five-parameter sensing using a single segment of optical fiber for the first time in the field of multiparameter optical fiber sensing.

ACKNOWLEDGMENT

Weiqiang Wang, Jingwei Lv, Jianxin Wang, Wei Liu, Qiang Liu, and Chao Liu are with the School of Physics and Electronic Engineering, Northeast Petroleum University, Daqing 163318, China (e-mail: msm-liu@126.com).

Miao Liu is with Shenzhen Key Laboratory of Ultra-Intense Laser and Advanced Material Technology, Center for Intense Laser Application Technology, and the College of Engineering Physics, Shenzhen Technology University, Shenzhen 518118, China.

Zao Yi is with the Joint Laboratory for Extreme Conditions Matter Properties, Southwest University of Science and Technology, Mianyang 621010, China.

Paul K. Chu is with the Department of Physics, the Department of Materials Science and Engineering, and the Department of Biomedical Engineering, City University of Hong Kong, Hong Kong, China.

REFERENCES

[1] R. C. Jorgenson and S. S. Yee, “A fiber-optic chemical sensor based on surface plasmon resonance,” *Sens. Actuators B, Chem.*, vol. 12, no. 3, pp. 213–220, Apr. 1993, doi: 10.1016/0925-4005(93)80021-3.

[2] T. Shen, W. Li, C. Liu, Y. Feng, X. Liu, and J. Gao, “D-shaped wide detection and high sensitivity dual-core photonic crystal fiber dual-parameter sensor,” *Phys. Scripta*, vol. 100, no. 7, Jul. 2025, Art. no. 075544, doi: 10.1088/1402-4896/ade7bf.

[3] H. Liang, Y. Feng, H. Liu, W. Han, and T. Shen, “High-performance PCF-SPR sensor coated with Ag and graphene for humidity sensing,” *Plasmonics*, vol. 17, no. 4, pp. 1765–1773, Aug. 2022, doi: 10.1007/s11468-022-01663-2.

[4] Y. Li, R.-L. Zhang, B.-H. Ding, and Q. Liu, “Research on voltage sensing characteristics of liquid crystal fully filled PCF with temperature compensation,” *Opt. Laser Technol.*, vol. 176, Sep. 2024, Art. no. 110986, doi: 10.1016/j.optlastec.2024.110986.

[5] M. D. C. Alonso-Murias, J. S. Velázquez-González, and D. Monzón-Hernández, “SPR fiber tip sensor for the simultaneous measurement of refractive index, temperature, and level of a liquid,” *J. Lightw. Technol.*, vol. 37, no. 18, pp. 4808–4814, Jun. 6, 2019, doi: 10.1109/JLT.2019.2921302.

[6] R. Zhang et al., “Voltage, thermal and magnetic field fiber sensors based on magnetic nanoparticles-doped photonic liquid crystal fibers,” *Opt. Exp.*, vol. 31, no. 16, pp. 25372–25384, 2023, doi: 10.1364/oe.492364.

[7] T. Huo, X. Jing, Z. Yin, T. Gao, and M. Song, “Compact three-channel photonic crystal fiber sensor based on surface plasmon resonance,” *Plasmonics*, vol. 20, no. 6, pp. 3085–3094, Sep. 2024, doi: 10.1007/s11468-024-02522-y.

[8] J. Wang, L. Wang, X. Su, R. Xiao, and H. Cheng, “Temperature, stress, refractive index and humidity multi parameter highly integrated optical fiber sensor,” *Opt. Laser Technol.*, vol. 152, Aug. 2022, Art. no. 108086, doi: 10.1016/j.optlastec.2022.108086.

[9] B. Li et al., “No-core optical fiber sensor based on surface plasmon resonance for glucose solution concentration and temperature measurement,” *Opt. Exp.*, vol. 29, no. 9, pp. 12930–12940, 2021, doi: 10.1364/oe.423307.

[10] C. Shao, H.-Y. Kim, J. Gong, B. Ding, D.-R. Lee, and S.-J. Park, “Fiber mats of poly(vinyl alcohol)/silica composite via electrospinning,” *Mater. Lett.*, vol. 57, nos. 9–10, pp. 1579–1584, Feb. 2003.

[11] H. Yang, C. Wang, G. Jin, and S. Yang, “Optical liquid-crystal magnetic field sensor with temperature compensation,” *IEEE Sensors J.*, vol. 24, no. 8, pp. 12259–12265, Apr. 2024, doi: 10.1109/JSEN.2023.3328186.

[12] T. Guo, X. Zheng, and P. Palffy-Muhoray, “The freedericksz transition in a spatially varying magnetic field,” *Crystals*, vol. 11, no. 5, p. 541, May 2021, doi: 10.3390/cryst11050541.

[13] S. Kim and X.-B. Pan, “Anisotropic nematic liquid crystals in an applied magnetic field,” *Nonlinearity*, vol. 33, no. 5, pp. 2035–2076, May 2020, doi: 10.1088/1361-6544/ab7103.

[14] J. Korec, K. A. Stasiewicz, L. R. Jaroszewicz, W. Piecek, and P. Kula, “Temperature and voltage sensing based on a tapered optical fiber device with the liquid crystal cladding,” *Opt. Fiber Technol.*, vol. 56, May 2020, Art. no. 102190, doi: 10.1016/j.yofte.2020.102190.

[15] H. Liu, C. Zhu, Y. Wang, C. Tan, and H. Li, “Polarization-dependent transverse-stress sensing characters of the gold-coated and liquid crystal filled photonic crystal fiber based on surface plasmon resonance,” *Opt. Fiber Technol.*, vol. 41, pp. 27–33, Mar. 2018, doi: 10.1016/j.yofte.2017.12.009.

[16] W.-L. Wang, Q. Liu, Z.-Y. Liu, Q. Wu, and Y.-Q. Fu, “Simulation of a temperature-compensated voltage sensor based on photonic crystal fiber infiltrated with liquid crystal and ethanol,” *Sensors*, vol. 22, no. 17, p. 6374, Aug. 2022, doi: 10.3390/s22176374.

[17] C. Zhao, L. Cai, and Y. Zhao, “An optical fiber electric field sensor based on polarization-maintaining photonic crystal fiber selectively filled with liquid crystal,” *Microelectronic Eng.*, vol. 250, Oct. 2021, Art. no. 111639, doi: 10.1016/j.mee.2021.111639.

[18] J. Li, S.-T. Wu, S. Brugioni, R. Meucci, and S. Faetti, “Infrared refractive indices of liquid crystals,” *J. Appl. Phys.*, vol. 97, no. 7, Apr. 2005, Art. no. 073501, doi: 10.1063/1.1877815.

[19] C. Liu et al., “Coreless optical fiber sensor based on surface plasmon resonance for simultaneous measurement of magnetic field and temperature,” *IEEE Sensors J.*, vol. 25, no. 12, pp. 21581–21588, Jun. 2025, doi: 10.1109/JSEN.2025.3562485.

[20] M. Song, X. Jing, and Z. Yin, “Simultaneous measurement of temperature and humidity using a dual-parameter sensor based on SPR and no-core fiber technology,” *Phys. Scripta*, vol. 99, no. 7, Jul. 2024, Art. no. 075524, doi: 10.1088/1402-4896/ad52d2.

[21] M. Song, X. Jing, P. Guo, Z. Yin, and S. Li, “SPR fiber optic sensor based on MMF-NCF doped with MgF_2 for dual-parameter measurement of temperature and humidity,” *Opt. Exp.*, vol. 33, no. 2, pp. 1869–1882, 2025, doi: 10.1364/oe.541155.

[22] Z. Zhu, L. Liu, Z. Liu, Y. Zhang, and Y. Zhang, “Surface-plasmon-resonance-based optical-fiber temperature sensor with high sensitivity and high figure of merit,” *Opt. Lett.*, vol. 42, no. 15, p. 2948, Aug. 2017.

Weiqiang Wang received the degree in electronic science and technology from Yanshan University, Qinhuangdao, China, in 2021. He is now pursuing the master’s degree in instrument science and technology with the School of Physics and Electronic Engineering, Northeast Petroleum University, Daqing, China.

He is mainly engaged in the research of fiber sensing technology and surface plasmon resonance fiber optic sensing technology.

Jingwei Lv, photograph and biography not available at the time of publication.

Jianxin Wang, photograph and biography not available at the time of publication.

Miao Liu, photograph and biography not available at the time of publication.

Wei Liu, photograph and biography not available at the time of publication.

Zao Yi, photograph and biography not available at the time of publication.

Qiang Liu, photograph and biography not available at the time of publication.

Paul K. Chu, photograph and biography not available at the time of publication.

Chao Liu received the bachelor’s degree in microelectronics technology from Heilongjiang University, Harbin, China, in 2002, and the master’s and doctor’s degrees in material physics and chemistry from Harbin Institute of Technology, Harbin, in 2004 and 2008, respectively.

He is a Visiting Scholar at the University of Western Australia, Perth, WA, Australia, and the City University of Hong Kong, Hong Kong. y. His research interests include optical fiber sensing, surface plasmon resonance, and nanofunctional materials.

Prof. Liu is a member of the Chinese Optical Society. He was an Associate Editorial Committee Member of the International SCI Journal Combinatorial Chemistry and High Throughput Screening, a Communication Reviewer of the National Natural Science Foundation of China, a Communication Reviewer of Beijing, Hebei, Zhejiang, and Heilongjiang Natural Science Foundation, and the Director of Heilongjiang Optical Society.